THE JOURNAL OF PHYSICAL CHEMISTRY C

Article

Cite This: J. Phys. Chem. C 2017, 121, 28435−28442

pubs.acs.org/JPCC

The Complexity of the CaF_2:Yb System: A Huge, Reversible, X-ray-Induced Valence Reduction

C. MacKeen,[†] F. Bridges,[*,†] L. Seijo,[‡] Z. Barandiarán,[‡] M. Kozina,[§] A. Mehta,[∥] M. F. Reid,[⊥] and J.-P. R. Wells[⊥]

[†]Physics Department, University of California, Santa Cruz, Santa Cruz, California 95064, United States

[‡]Departamento de Química, Instituto Universitario de Ciencia de Materiales Nicolás Cabrera, and Condensed Matter Physics Center (IFIMAC), Universidad Autónoma de Madrid, 28049 Madrid, Spain

[§]Linac Coherent Light Source and [∥]Stanford Synchrotron Radiation Lightsource, SLAC National Accelerator Laboratory, Menlo Park, California 94025, United States

[⊥]Dodd-Walls Centre for Photonic and Quantum Technologies and School of Physical and Chemical Sciences, University of Canterbury, PB 4800, Christchurch 8140, New Zealand

Supporting Information

ABSTRACT: Lanthanides are multivalent chemical systems whose luminescence activates numerous optical devices. Their multivalent nature sets a complex scenario that challenges widespread single-valent-ion models. Here we study the complexity inherent in the 2+/3+ mixed-valence nature of Yb in CaF_2. We report X-ray absorption spectroscopy of CaF_2:Yb that shows a maximal, huge Yb^{3+} X-ray-induced valence reduction at 200 K for low Yb concentration (0.01%) samples, which reverts to the initial state upon warming to 300 K. Although reduction doubles the number of Yb^{2+} ions, the anomalous emission that is normally observed at low temperatures completely disappears and never recovers. Surprisingly, however, after annealing at 900 K, some anomalous emission is again observed below 150 K. Under X-ray exposure electrons are ejected from the F^- ions, including charge compensating interstitials, F_i^-. Removing an electron from F_i^- leaves a neutral atom which appears metastable. *Ab initio* calculations of the F_i^--to-Yb^{3+} electron transfer reveal there is a critical dopant−compensator distance below which reoxidation is spontaneous and above which it is not. This, together with temperature-dependent F_i^0 and F_i^- mobilities, and the interpretation of the anomalous emission as an Yb^{2+}-to-Yb^{3+} electron transfer provide a model for interpreting the complex experimental observations.

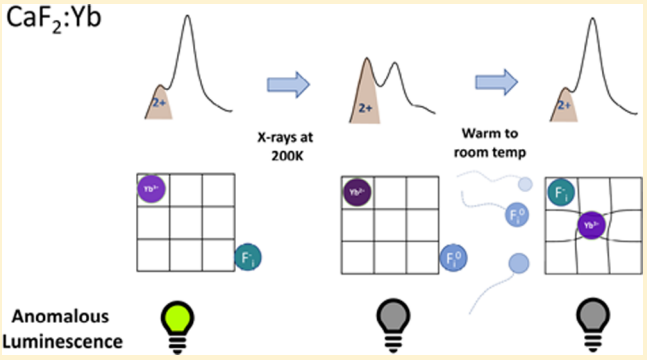

INTRODUCTION

The interest in the trivalent lanthanide ions as solid-state laser activators that started in the 1960s rapidly expanded to the divalent lanthanides as it was shown that all ions from Ce^{3+} to Yb^{3+} could be partially reduced by γ-rays when doped in suitable host crystals like CaF_2.[1] However, some drawbacks followed the initial efforts, and Yb-doped CaF_2 is an archetypical example: Whereas CaF_2:Yb^{3+} has become a very successful high-power diode-pumped IR laser near 1050 nm (broad band emission over 920−1100 nm),[2−5] CaF_2:Yb^{2+} had to be ruled out as a laser because an anomalous emission (AE, a slow, extremely broad, and red-shifted emission near 540 nm, previously associated with Yb^{2+}) was found after UV and higher energy excitation.[5−8] The physics behind the AE is not yet clear: A model to describe the AE in a variety of lanthanide-doped crystals was developed in the 1980s by McClure and others,[9−11] in which the optical center is thought to be an impurity trapped exciton (ITE) at the divalent lanthanide. However, *ab initio* calculations could not support the ITE hypothesis and showed that the AE can be identified with an Yb^{2+}/Yb^{3+} intervalence charge transfer (IVCT) luminescence instead.[12] The IVCT hypothesis is based on the 2+/3+ multivalent nature of Yb-doped CaF_2 and draws a much more complex scenario for the AE than that of the ITE hypothesis.

The multivalent nature of Yb in CaF_2 at low concentrations has been experimentally proven only recently when it has been possible to obtain fractions of Yb^{2+}, $f(2+)$, and Yb^{3+}, $f(3+)$, from X-ray absorption near edge structure (XANES) analyses for different global Yb concentrations in CaF_2.[13,14] The XANES experiments and corresponding UV−vis emission spectra have shown evidence that the ITE model of the AE breaks down in this system since the emission intensity is far from proportional

Received: September 13, 2017
Revised: November 16, 2017
Published: November 20, 2017

DOI: 10.1021/acs.jpcc.7b09161
J. Phys. Chem. C 2017, 121, 28435−28442

to the Yb^{2+} concentration.[14] On the other hand, this trend is compatible with the IVCT luminescence interpretation if the Yb^{2+}-to-Yb^{3+} electron transfer is more efficient when the Yb^{3+} centers are nonlocally compensated and hence cubic.[12,14,15]

In this work we study the complexity inherent in the multivalent nature of CaF_2:Yb. For concentrations above roughly 0.1%, most of the Yb is in a 3+ state which requires a charge compensating defect such as interstitial F_i^- or O^{2-} (our samples are grown in an O-free environment with a slight excess of F, so no O^{2-} present).[16] There are several Yb^{3+} defects with different symmetries,[16−18] depending on the type and location of these charge-compensating defects. At lower concentrations (<0.1%) a small fraction (<30%) of Yb is in the Yb^{2+} state, and this fraction increases at lower Yb concentrations. The effects that X-ray exposure at different temperatures and subsequent thermal treatment have on the 2+/3+ valence conversion, the dopant local structures, and the Yb anomalous emission in dilute CaF_2:Yb single crystals are studied using a combination of XANES, X-ray absorption fine structure (EXAFS), and UV−vis absorption and emission spectra plus *ab initio* calculations of the redox reaction

$$F_i^- + Yb^{3+} \underset{T}{\overset{\text{X-ray}}{\rightleftharpoons}} F_i^0 + Yb^{2+} \quad (1)$$

whose relevance in X-ray-induced reversible reduction of trivalent rare earths was first proposed by Merz and Pershan.[19,20] The results show a novel, huge, and maximal reduction of Yb in CaF_2:0.01%Yb samples from mostly 3+ to mostly 2+ after a long exposure at 200 K (from $f(2+) = 0.3$ to $f(2+) = 0.7$); however, even after 200 min, the fraction $f(2+)$ is still increasing slightly. Although the huge reduction is stable at low temperatures, reoxidation to the initial 2+/3+ fractions follows after warming to room temperature (hours) and rapidly (minutes) at 320 K. The ability to reversibly change the Yb valence from 3+ to 2+ provides a straightforward means of investigating changes in the local Yb−F bond lengths. As expected, the Yb−F bond is shorter when Yb is in the 3+ state, but there is little change in the second neighbor Yb−Ca distance. The AE of Yb that is observed in the as-grown samples is lost after the X-ray exposure and throughout the thermal reoxidation process, and, surprisingly, is only recovered after annealing at high temperature (900 K), even though annealing does not change the Yb^{2+} concentration or the 2+/3+ fraction. The *ab initio* calculations reveal the existence of a critical distance between the dopant and the interstitial fluorine ions below which the F_i^0−Yb^{2+} hole−electron recombine spontaneously and above which the F_i^0−Yb^{2+} pair is metastable. This central feature, combined with temperature-dependent F_i^0 and F_i^- mobilities, provides a model for interpreting the complex experimental observations.

EXPERIMENTAL AND THEORETICAL METHODS

EXAFS and XANES data at the Yb L_{III} edge were collected on beamline 11-2 at SSRL using an Oxford helium flow cryostat, out to $k = 11$ Å^{-1}. The slits were 1.0 mm × 5.0 mm, providing an energy resolution of 1.3 eV. The data were reduced and analyzed using RSXAP[21] which follows standard procedures; examples of the *k*-space data are shown in the Supporting Information. These data were Fourier transformed (FT) to real space using an FT window 3.5−10.0 Å^{-1}, with a Gaussian window rounding of 0.3 Å^{-1}.

The CaF_2:Yb samples were grown as described in ref 22. A thin, polished, single crystal disk (10 mm in diameter, 1 mm thick) with 0.01% Yb was used to collect the XANES and EXAFS data in fluorescence mode (sample at 45° to beam), using a 100 element fluorescence detector. Such a transparent sample is needed to also monitor UV-induced emission. However, because of Bragg reflections from the single crystal, some detector channels had large (Bragg) spikes at some energies in a scan, and those channels had to be removed. Further, since Bragg peaks are sensitive to the single crystal orientation, the appropriate channels had to be determined each time a sample was mounted. Typically 50−70 channels had no Bragg spikes and were used for the XANES and EXAFS data collection. UV excitation at SSRL used an LED source at 365 nm (near the top of the UV absorption peak). The UV source was not focused and provided a wide beam about 10 mm in diameter. The anomalous emission was monitored using a Ocean Optics USB spectrometer.

The diabatic potential energy surfaces for F_i^-−Yb^{3+} and F_i^0−Yb^{2+} pair states were computed using the results of independent embedded cluster calculations on cubic $(F_iF_8)^{9-}$, $(YbF_8)^{5-}$, $(F_iF_8)^{8-}$, and $(YbF_8)^{6-}$ clusters in CaF_2; the YbF_8 clusters were calculated in ref 12. The relativistic second-order Douglas−Kroll−Hess Hamiltonian[23−25] was used including all cluster electrons. Quantum mechanical *ab initio* embedding model potentials (AIMP)[26,27] obtained for CaF_2[12] were used to represent the effects of all ions within a cube of 7 × 7 × 7 unit cells plus additional point charges[28] around the embedded clusters. The relativistic atomic natural orbital basis set (ANO-RCC)[29] F (14s9p4d3f2g) [5s4p3d] was used for all fluorines supplemented with Ca (20s15p) [1s1p] second-neighbor orthogonalization functions.[12] Multireference wave functions and energies were obtained in two steps of (i) complete active space self-consistent field (CASSCF)[30−34] and (ii) multistate second-order perturbation method (MS-CASPT2) calculations.[34−38] Spin−orbit coupling was included in the YbF_8 clusters[12] and neglected in the F_iF_8 clusters. More details are given in the Supporting Information. The suite of programs MOLCAS was used for all calculations.[39]

RESULTS

XANES. In initial measurements on CaF_2:Yb, no obvious X-ray-induced valence change occurred in a few successive scans at 300 K during setup of the fluorescence detector (see Experimental and Theoretical Methods section) or in scans at low temperatures below 80 K. A more careful evaluation later showed that small valence changes do occur at both 300 and 80 K after many scans, but the effects are small—a few percent—as observed earlier by Merz.[19] However, in one run, multiple XANES scans were collected during cooldown, and a large change in the edge was noted between about 250 and 150 K. Further investigation showed that a large valence reduction only occurs near 200 K and is extremely unusual. Reversible valence changes may occur when samples are damaged;[40,41] also, large increases in valence have been observed under high pressure,[42] but not a valence decrease.

The normalized XANES at 200 K for 0.01% Yb are plotted in Figure 1 for various X-ray exposure times (using multiple scans at the Yb L_{III} edge). Note that the "zero" minute scan is the start of these measurements, but the sample already had some exposure and Yb is slightly reduced. Also, note that the short time to scan the Yb XANES (3−4 min) has little effect on the relative amplitudes of the 2+ and 3+ peaks. Once Yb has been mostly reduced to Yb^{2+}, it is relatively stable at low temperatures for long periods of time—with small changes

DOI: 10.1021/acs.jpcc.7b09161
J. Phys. Chem. C 2017, 121, 28435−28442

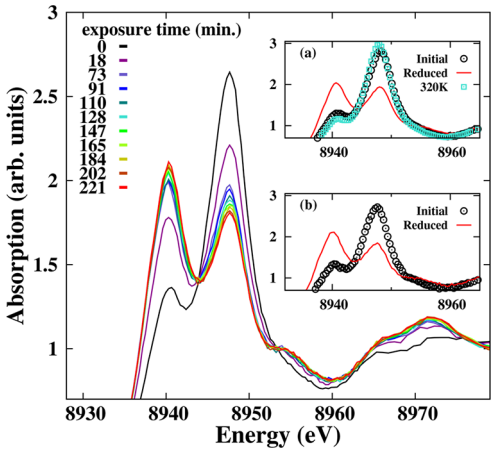

Figure 1. Evolution of Yb L_{III} XANES spectra as a function of X-ray exposure time t for multiple scans at 200 K for CaF_2:Yb (0.01%). At t = 0, the sample had some X-ray exposure and Yb was already slightly reduced. The 8942 eV peak is associated with Yb^{2+} and the 8949 eV peak with Yb^{3+}. Over ∼3 h, the valence changes from mostly 3+ to mostly 2+. Note also the changes in the EXAFS range above 8955 eV. Insets: (a) XANES from a different experimental run; little X-ray exposure (open black circles), after X-ray exposure at 200 K (∼4 h, red) from multiple EXAFS scans at the Yb L_{III} and after heating to 320 K (green squares). The scan at 320 K has slightly less Yb^{2+} than the initial scan. (b) Similar changes when another fresh sample is exposed to X-rays at 7940 eV, 1 keV below the Yb L_{III} edge. The same valence reduction occurs over a time period of 200 min (red solid curve).

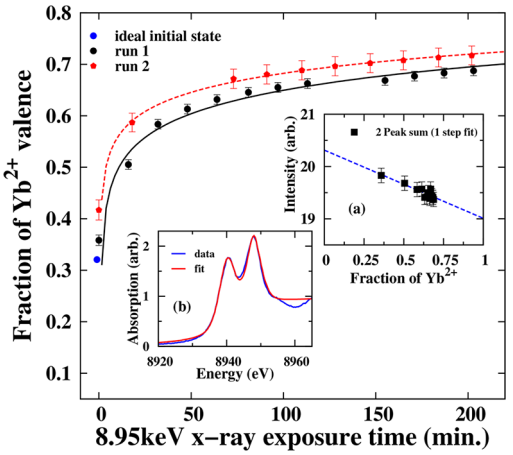

Figure 2. Fraction of Yb^{2+} (f(2+)) as a function of X-ray exposure time at 200 K for 0.01% Yb; f(2+) changes from about ∼0.3 to 0.7 and varies roughly logarithmically with t (lines). Insets: (a) sum of the integrated areas for the two peaks as a function of Yb^{2+} fraction. This sum decreases slightly as the valence decreases from mostly 3+ to mostly 2+. (b) An example of a fit of the XANES to two pseudo-Voigt peaks plus a step function.

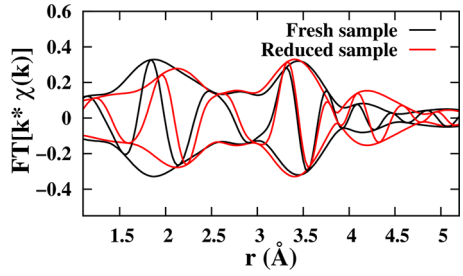

Figure 3. EXAFS r-space data at 10 K for a fresh sample and after maximum valence reduction. Peaks in the EXAFS data correspond to shells of neighbors surrounding the Yb defect. The fast oscillatory function is the real part R of the Fourier transform (FT) while the amplitude functions are $\pm\sqrt{R^2 + I^2}$; I is the imaginary part of the FT. There is a large increase in the distance (∼0.15 Å) for the first peak near 1.9 Å, for the valence reduced sample (red trace), compared to the as-made sample (black). In contrast for the second Yb−Ca peak, the pair distance changes very little upon valence reduction.

over 8 h. In addition, a subsequent experiment showed that valence reduction is also achieved at 7940 eV, 1 keV below the Yb L_{III} edge (Figure 1b); i.e., no excitation of the Yb ions is required. Perhaps even more surprising is that this valence reduction is rapidly reversible (minutes) by heating to 320 K (see Figure 1a).

To determine the fractions (f(2+) and f(3+)) of Yb^{2+} and Yb^{3+}, the XANES data were fit to a sum of two pseudo-Voigt peaks for the 2+ and 3+ lines plus a broadened step function for the main edge. From initial trials the average widths for both peaks and the step function were determined and then fixed in the final fits. No constraints on the integrated peak amplitudes for the two peaks were used. An example of a fit is shown in Figure 2b. From the fit the areas under each peak were determined; initial fits showed that the sum of these two areas decreased slightly as f(2+) increased. Consequently, the matrix element for Yb^{2+} is slightly smaller than for Yb^{3+}, and an iterative fit was required to first determine the ratio of matrix elements and then extract f(2+) (see Supporting Information for details). The fraction f(2+) is plotted as a function of time in Figure 2 for two different experimental runs; it varies from roughly 0.3 to 0.7 for this sample.

In Figure 2a, the sum of the integrated intensities is plotted as a function of f(2+) after the iterative procedure converged; extrapolating the straight line fit to pure Yb^{2+} and Yb^{3+} gives the relative ratio of the matrix elements p_i for Yb^{2+} and Yb^{3+}; p_{2+}/p_{3+} ∼ 0.93. This ratio was used in determining the fraction f(2+) and is closer to 1.0 than the value, p_{2+}/p_{3+} = 0.65, used by Hughes-Currie et al.,[22] based on results for Eu^{2+} and Eu^{3+} in solution.[43] It is not clear that solution results, for which the environment about the ion is quite different, are transferable to a solid.

EXAFS. EXAFS r-space scans at the Yb L_{III} edge, for data collected at 10 K, are shown in Figure 3 for the two valence states. These measurements probe the differences in local structure around Yb^{2+} and Yb^{3+} configurations, where Yb occupies a Ca site. In the CaF_2 structure there are 8 nearest-neighbor F, 12 second neighbor Ca, and 24 third neighbor F atoms about the Yb atoms. However, the results for the first peak in Figure 3 indicate a large increase in nearest-neighbor Yb−F bond length for Yb^{2+} (red; reduced sample) compared to Yb^{3+} (black; fresh sample).

In order to investigate the large difference between the r-space EXAFS data before and after X-ray exposure, we fit the data[21] to a sum of theoretical EXAFS functions for the dominant scatter paths (calculated with FEFF7[44]) using the following model: two Yb−F peaks corresponding to pure Yb^{2+} and Yb^{3+} with r's ∼ 2.40 and 2.25 Å; a Yb−Ca second neighbor peak near r = 3.867 Å; a long third neighbor Yb−F peak near 4.53 Å, plus multiscattering peaks in the range 3.5−4.5 Å. See the Supporting Information for additional details and the individual components in each fit.

The fits for the fresh and fully reduced samples are shown in Figure 4, and the fit parameters are tabulated in Table1. The

DOI: 10.1021/acs.jpcc.7b09161
J. Phys. Chem. C 2017, 121, 28435−28442

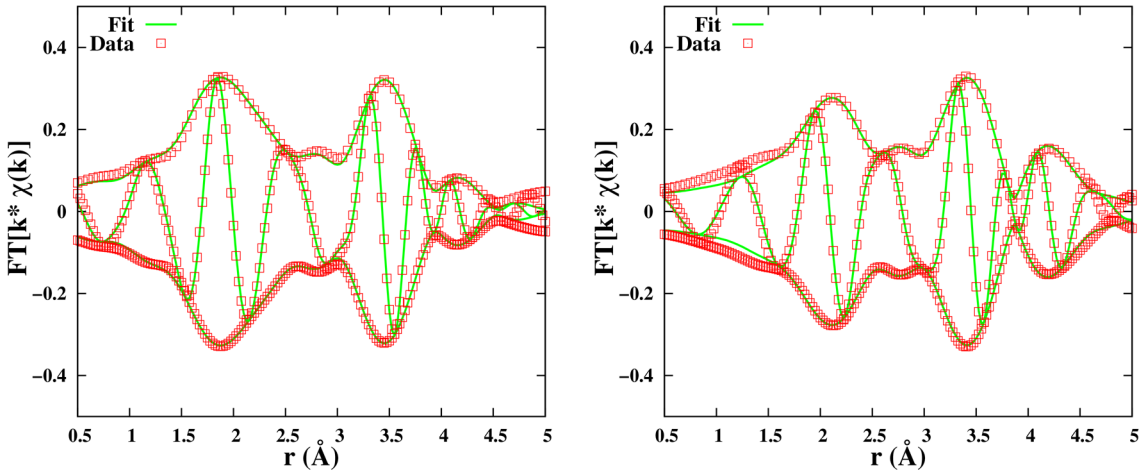

Figure 4. Fits of the real space data for the fresh sample (left) and the valence reduced sample (right) using the model discussed in the text. The Fourier transform window is 3.5−10.0 Å^{-1}, with a 0.3 Å^{-1} Gaussian rounding; the fitting range in *r*-space is 1.5−4.7 Å.

Table 1. Results of the EXAFS Fits for the Fresh and Valence Reduced Samples[a]

pair	amplitude	host (Å)	position (Å)	σ^2
		fresh sample		
Yb^{3+}−F	5.6(1)	2.366	2.250(4)	0.0063(8)
Yb^{2+}−F	2.4(1)	2.366	2.401(10)	0.0031(5)
Yb−Ca	12	3.863	3.890(2)	0.0037(2)
Yb−F	24	4.530	4.488(3)	0.0113(2)
		reduced sample		
Yb^{3+}−F	2.4(3)	2.366	2.250(4)	0.0122(14)
Yb^{2+}−F	5.6(3)	2.366	2.401(10)	0.0048(10)
Yb−Ca	12	3.863	3.874(5)	0.0031(4)
Yb−F	24	4.530	4.537(7)	0.0026(6)

[a]Yb^{2+}−F and Yb^{3+}−F are for sites with valence 2+ and 3+, respectively. Fit range in *r*-space, 1.5−4.7 Å. The amplitude is the degeneracy for each shell but is split for the first shell as a result of the two valence states. σ^2 is the correlated Debye−Waller factor where σ is the width of the pair distribution function. The errors show the reproducibility of the data in fits of multiple scans. Including systematic effects the errors for *r* are ∼0.01 Å for the first two neighbors and up to 0.02 Å for further peaks. Because of the correlations between N and σ, systematic uncertainty is typically 10−15% for these parameters. S_0^2 = 1.0.

main results are that the closest Yb−F pair is contracted for Yb^{3+} and slightly expanded for Yb^{2+} relative to the Ca−F pair in the host material, with a total splitting of 0.15 Å, while the second neighbor pair (Yb−Ca) has almost the same distance for both valence states (difference ∼0.02 Å). Both results agree well with early estimations[9,11] for the two valence states and with *ab initio* calculations[12] for which the bond lengths and their splitting are 2.33 Å (Yb^{2+}), 2.20 Å (Yb^{3+}); and 0.13 Å, respectively; the bond length of Yb^{2+}−F becomes even closer to the EXAFS value if the representation of the second neighbors is improved: 2.37 Å. In addition, the third (Yb−F) neighbors are at the same distance as for CaF_2 when Yb is 2+, but for 3+, the further F atom is pulled in slightly, by ∼0.04 Å. A similar local distortion about a higher valence dopant was also observed in Zn-doped $LiNbO_3$.[45] The environment about Yb^{3+} above 4 Å is also more disordered; however, the decrease in amplitude from 4 to 4.5 Å for the fresh sample also depends on changing interference with multiscattering peaks and is discussed in the Supporting Information. From the EXAFS analysis, the fraction *f*(2+) in the as-made sample is about 0.30, while that for the strongly reduced sample is 0.70, very close to the fractions obtained from the XANES analysis above.

Anomalous Emission. Perhaps the most surprising result is that after extensive X-ray exposure plus heating to room temperature, no yellow-green anomalous emission was observed at 80 K in subsequent measurements, although the XANES were nearly identical to the unexposed sample, and the UV absorption did not change (see Supporting Information).

In a separate experiment carried out 8 months after the last X-ray experiments, the emission spectra for two samples that had never been exposed to X-rays were compared with that for the X-ray exposed sample. The results are plotted in Figure 5;

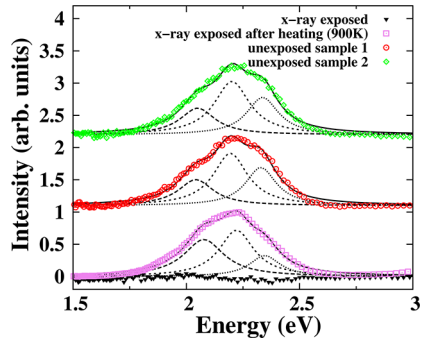

Figure 5. Normalized plots (80 K) of the yellow-green emission for two samples never exposed to X-rays (red circle; green diamond), the sample with extensive X-ray exposure (black, not normalized), and the X-ray-exposed sample after annealing at 900 K (square purple symbols). The nearly flat (black) trace for the X-ray-exposed sample has a remnant from the background subtraction. Each scan can be fit to a sum of three Lorentzians (see Supporting Information); importantly, the relative amplitudes of the components for the annealed sample are different.

the anomalous emission spectra for the samples not exposed to X-rays were essentially identical, with a peak near 2.2 eV (∼560 nm), but the X-ray exposed sample had no clear emission peak, only a remnant of the background subtraction remains. Upon annealing at 900 K (cooled slowly for ∼2 h), the yellow-green emission was again observed as shown by the square symbols on Figure 5, but the shape of the spectrum has changed. Each scan can be fit to a sum of three Lorentzians as shown in Figure

DOI: 10.1021/acs.jpcc.7b09161
J. Phys. Chem. C 2017, 121, 28435−28442

5; the relative weights of these three components are different for the annealed sample, suggesting a distribution of slightly different emission centers and likely different local environments.

Theoretical Calculations. To begin to understand this very complex behavior, *ab initio* calculations have been carried out with charge-compensating interstitial F ions at various distances from an Yb^{3+} dopant. The first few interstitial sites are illustrated in Figure 6.

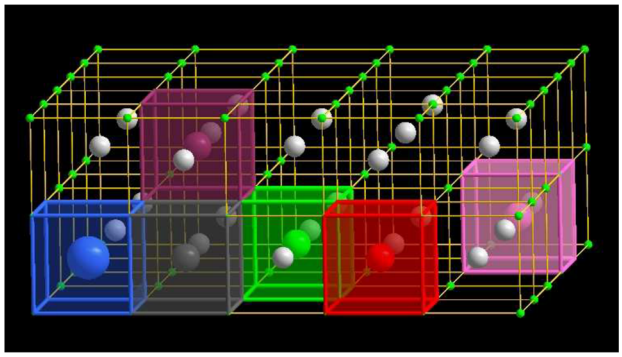

Figure 6. Partial representation of a fluorite crystal structure surrounding one Yb dopant ion in blue, located in the YbF_8 cube that is shaded in blue. Some of the Ca^{2+} ions located at the center of every other cube are plotted in light gray; crystal fluoride ions in green are located at the vertices of all cubes. Five cubes around interstices are shaded in colors (dark gray, violet, green, red, and magenta); at their center an interstitial fluoride ion F_i^- is indicated in the same color. The distance from the Yb ion (in blue) and each of the interstitial fluorides plotted are d_{F_i-Yb} = 2.73 (dark gray), 4.73 (violet), 6.11 (green), 8.19 (red), and 13.7 Å (magenta). Each *ab initio* calculation comprises the YbF_8 cluster and one of the five F_iF_8 cubes embedded in the fluorite crystal. See text and Figure 7 and Figure S5 for details.

The results of these calculations are plotted in Figure 7 for the electron transfer reaction between interstitial fluorine and ytterbium ions (eq 1). We have considered six interstitial sites around an Yb^{3+} ion (see Figure 6) and calculated the energies at each of these different F_i–Yb distances (d_{F_i-Yb}) using wave-function-based embedded cluster methods of quantum chemistry. Further details about the calculations are given in the Supporting Information. The following can be deduced from them.

(A) The dopant–compensator distance determines the stability of the X-ray-induced reduction. The diabatic configuration coordinate energy diagrams of Figure 7 show there is a critical F_i–Yb distance ($d^{critical}_{F_i-Yb} \simeq 8.19$ Å) up to which the backward oxidation of Yb is spontaneous (F_i^0–Yb^{2+} energy curves above the red line with energy minima are above the blue line for $^2F_{7/2}$) and beyond which the X-ray-induced reduction is metastable (F_i^0–Yb^{2+} energy curves below the red line for which the energy minima are below the blue line for $^2F_{7/2}$). Then, we can write for the locally compensated Yb^{3+}_{LC}

$$F_i^- + Yb^{3+}_{LC} \overset{\text{X-ray}}{\rightleftharpoons} F_i^0 + Yb^{2+}, \quad d_{F_i-Yb} \le d^{critical}_{F_i-Yb} \tag{2}$$

and for the nonlocally compensated Yb^{3+}_{NLC}

$$F_i^- + Yb^{3+}_{NLC} \xrightarrow{\text{X-ray}} F_i^0 + Yb^{2+}, \quad d_{F_i-Yb} > d^{critical}_{F_i-Yb} \tag{3}$$

This central message is compatible with the diabatic approximation; in other words, the message should hold even if the diabatic approximation were overcome (cf. Supporting Information).

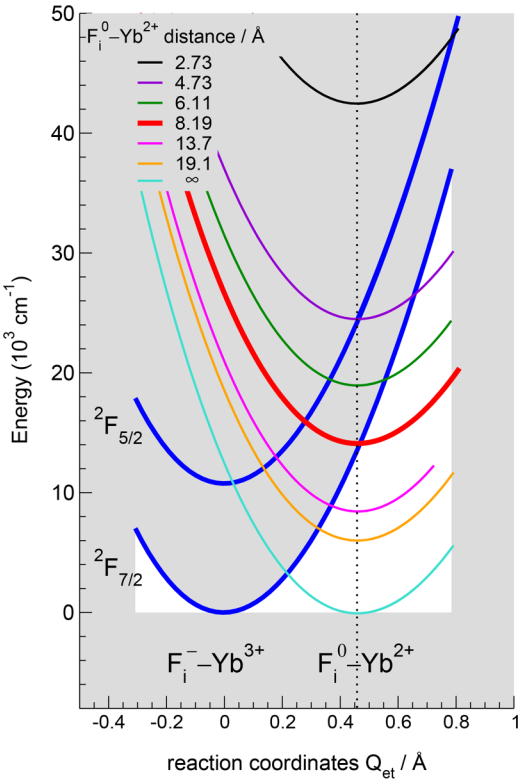

Figure 7. Diabatic configuration coordinate energy diagrams for F_i^-/Yb^{3+} electron transfer in CaF_2 at different F_i–Yb distances are plotted together in this figure. The diagrams show the existence of a critical distance $d^{critical}_{F_i-Yb} \simeq 8.19$ Å. For $d_{F_i-Yb} < d^{critical}_{F_i-Yb}$ the F_i^0–Yb^{2+} minima lie on the left and above the F_i^-–Yb^{3+} ground state in the gray region; hence, the hole–electron F_i^0–Yb^{2+} pair spontaneously recombines; for $d_{F_i-Yb} > d^{critical}_{F_i-Yb}$ they lie on the right and below the F_i^-–Yb^{3+} ground state curve, in the white region; hence, the F_i^0–Yb^{2+} hole–electron pair state is metastable. Note that when F_i^0 moves away from (or toward) Yb^{2+} after reduction, the energy curve of the F_i^0–Yb^{2+} hole–electron pair shifts down (or up). The F_i^0–Yb^{2+} ground-state minima are connected with a vertical dotted line for comparisons. At very large separations the energy for the F_i^0–Yb^{2+} hole–electron pair is only slightly higher than that for the F_i^-–Yb^{3+} ground state and is not seen on this scale (see Supporting Information for more details).

This result is in agreement with extensive experimental data that suggest that only those rare-earth trivalent ions in cubic sites are reduced to the divalent state in CaF_2-doped crystals.[19]

(B) There is a temperature, T_{Red}, at which X-ray-induced reduction is maximal. In order to understand the effects of X-ray exposure at different temperatures on Yb^{3+}_{LC} and Yb^{3+}_{NLC} centers, we combine now the results of the *ab initio* calculations with the expected temperature dependent mobility of F_i^0 holes through the crystal, inferred from experiments (cf. refs 19 and 46 and references therein).

(i) Yb^{3+}_{LC} centers at temperatures below a threshold, $T \le T_{Red}$: If, during the X-ray-induced reduction process (forward reaction of eq 2), some F_i^0 move away from Yb^{2+}, surpassing the critical distance $d^{critical}_{F_i-Yb}$, their corresponding F_i^0–Yb^{2+} hole–electron pairs would be stabilized at an energy curve lower than the red one. However, those staying close to Yb^{2+} ions will reoxidize back to Yb^{3+}_{LC}. Thus, the initial Yb^{3+}_{LC} centers would be

DOI: 10.1021/acs.jpcc.7b09161
J. Phys. Chem. C 2017, 121, 28435–28442

partly reduced and partly reoxidized, leading to the following Yb^{3+} defects balance:

$$\{Yb^{3+}_{LC}\}_{T\le T_{Red}} \xrightarrow{\text{X-ray}} \{Yb^{3+}_{LC} + Yb^{2+}\}_{T\le T_{Red}} \quad (4)$$

where initial refers to the sample before X-ray exposure.

(ii) Yb^{3+}_{NLC} centers at temperatures below a threshold, $T \le T_{Red}$: Correspondingly, if during the X-ray reduction of eq 3, some of the F_i^0 move closer to the Yb^{2+} ions and reach the $d_{F_i-Yb} \le d^{critical}_{F_i-Yb}$ range, the energies of their corresponding $F_i^0-Yb^{2+}$ pairs would be above the red energy curve, so that a spontaneous nonradiative electron−hole recombination would reoxidize those divalent Yb ions to Yb^{3+}_{LC}. The remaining Yb^{2+} ions would not have any F_i^0 sufficiently close and would remain stable. Thus, the initially cubic Yb^{3+}_{NLC} centers would be partly reduced and partly distorted by local compensation:

$$\{Yb^{3+}_{NLC}\}_{T\le T_{Red}} \xrightarrow{\text{X-ray}} \{Yb^{3+}_{LC} + Yb^{2+}\}_{T\le T_{Red}} \quad (5)$$

Altogether, the outcomes of eqs 4 and 5 are (a) an X-ray induced Yb reduction and (b) a decrease of cubic, nonlocally compensated Yb^{3+} centers.

However, given that the F_i^0 mobility increases with temperature, the net effects of Yb reduction and decrease of Yb^{3+}_{NLC} cubic centers should strengthen at first ($T < T_{Red}$), reach a maximum at a given temperature ($T = T_{Red}$), and diminish again as T increases further ($T > T_{Red}$). The latter corresponds to temperatures where the F_i^0 mobility is high enough so that F_i^0 would always get close to some other Yb^{2+} center to recombine, thus making reoxidation to locally compensated Yb^{3+}_{LC} most likely

$$\{Yb^{3+}_{LC} + Yb^{3+}_{NLC}\}_{T>T_{Red}} \xrightarrow{\text{X-ray}} \{Yb^{3+}_{LC}\}_{T>T_{Red}} \quad (6)$$

All this is consistent with the huge reduction observed in the XANES spectra from $f(2+) = 0.3$ to $f(2+) = 0.7$ for exposure at 200 K (T_{Red} = 200 K) and the small changes in the XANES spectra upon exposures below 80 K ($T < T_{Red}$) and at 300 K ($T > T_{Red}$). This also explains the small reduction achieved at 77 K by Merz and Pershan ($T < T_{Red}$).[19]

It should be noted that X-ray-induced defects in CaF_2 could make net X-ray-induced ytterbium reduction even more unlikely at low temperatures: Görlich et al.[46] have suggested that X-ray exposure favors an increase in the concentration of Frenkel defects (anion vacancies plus interstitial fluoride ions) and ionization of interstitial and crystal fluoride ions, which are less mobile the lower the temperature is. This could affect the balance we have just discussed making the reoxidation of the Yb^{2+} produced by X-rays (eq 3) more likely in the presence of nearby metastable F_i^0 or F^0 centers.

(C) Both X-ray exposure and warming after X-ray exposure enhance local compensation and quench Yb anomalous emission: The decrease in the number of cubic centers by X-ray exposure, expressed in eq 5 for $T = T_{Red}$, should result in quenching of Yb AE as long as the AE is interpreted as a radiative electron transfer between Yb^{2+} and a cubic, nonlocally compensated Yb^{3+}_{NLC} center, i.e., as Yb^{2+}/Yb^{3+}_{NLC} IVCT luminescence. This is consistent with the experimental fact that the AE was no longer observed at low temperatures after X-ray exposure at 200 K even though the number of Yb^{2+} ions nearly doubled by the X-ray-induced reduction (Figure 5).

Besides, warming to room temperature (RT) after exposure at T_{Red} = 200 K should increase F_i^0 mobility and favor their encounters with Yb^{2+} and reoxidation to locally compensated Yb^{3+}_{LC}:

$$\{Yb^{3+}_{LC}\}_{T_{Red}} \xrightarrow{\text{X-ray}} \{Yb^{3+}_{LC} + Yb^{2+}\}_{T_{Red}} \xrightarrow{\text{warming}} \{Yb^{3+}_{LC}\}_{RT}$$

$$\{Yb^{3+}_{NLC}\}_{T_{Red}} \xrightarrow{\text{X-ray}} \{Yb^{3+}_{LC} + Yb^{2+}\}_{T_{Red}} \xrightarrow{\text{warming}} \{Yb^{3+}_{LC}\}_{RT}$$

(Note this is basically the same scenario as discussed above for exposures at $T > T_{Red}$; eq 6.) This means, again, that the AE should be quenched if it is an Yb^{2+}/Yb^{3+}_{NLC} IVCT luminescence. This is consistent with the facts that after warming to 320 K reoxidation was observed—from $f(2+) = 0.7$ back to 0.3—but the AE, observable in the initial unexposed sample, was not recovered.

(D) Annealing at high temperatures increases nonlocal compensation and recovers Yb anomalous emission: It has been shown that annealing at 1000−1200 °C followed by rapid quenching to room temperature induces full cubic nonlocal charge compensation of trivalent lanthanides in fluorite[15,47] and fluorite-type crystals;[48] this symmetrizing effect is attenuated with smaller annealing temperatures and smaller cooling gradients, in which case conversion to cubic centers would be only partial:[47,48]

$$\{Yb^{3+}_{LC}\}_{RT} \xrightarrow{\text{annealing}} \{Yb^{3+}_{NLC} + Yb^{3+}_{LC}\}_{RT} \quad (7)$$

Thus, the reappearance of some Yb^{3+}_{NLC} cubic centers should result in recovery of the Yb^{2+}/Yb^{3+}_{NLC} IVCT luminescence, in agreement with the experimentally observed recovery of the AE after annealing at 900 K (~600 °C) plus cooling to room temperature over ~2 h.

Obviously, the redistributions associated with the mobility of interstitial F_i^0 and F_i^- centers along the whole process of exposure plus heating mean that the final and initial Yb^{3+}_{LC} and Yb^{3+}_{NLC} distributions are not identical. This is consistent with the slight change in shape of the anomalous emission band recovered after annealing (Figure 5).

(E) The X-ray-induced reversible reduction of Eu^{3+} and Yb^{3+} should be very similar.The energy difference between the $F_i^- - Yb^{3+}$ and $F_i^0-Yb^{2+}$ ground-state minima plotted in Figure 7 for different d_{F_i-Yb} distances depends on (minus) the ionization potential of Yb^{2+} in CaF_2.[49,50] The ionization potentials of Yb^{2+} and Eu^{2+} are known to differ only by ~1000 cm^{-1};[51−53] therefore, the F_i^-/Yb^{3+} and F_i^-/Eu^{3+} configuration coordinate energy diagrams should be basically the same, as in Figure 7, and the maximal and huge reversible reduction observed in CaF_2:Yb should be also expected for CaF_2:Eu.

DISCUSSION AND CONCLUSIONS

The above experiments show that the valence of dilute Yb in CaF_2 can be dramatically changed via X-ray exposure near 200 K and remains stable at low temperatures for many hours. Further, this change is reversible upon warming to room temperature and allows a study of the local structure differences around Yb^{3+} and Yb^{2+} ions. The EXAFS on the fresh and highly reduced samples shows a large decrease in Yb−F bond length from Yb^{2+} to Yb^{3+}, but changes in the distances to further neighbors are small.

A reduction in valence from mostly 3+ to mostly 2+ requires a change in the charge compensation that remains metastable at low temperatures. In CaF_2 charge compensation is achieved via interstitial F_i^- ions; if electrons are removed during X-ray exposure, some of these defects may become neutral—F_i^0.

DOI: 10.1021/acs.jpcc.7b09161
J. Phys. Chem. C 2017, 121, 28435−28442

Theoretical calculations for $Yb^{2+}-F_i^0$ pairs show that there is a critical separation, above which F_i^0 is stable but below which Yb^{2+} is reoxidized to form $Yb^{3+}-F_i^-$ pairs. This illustrates the importance of understanding the role of the charge-compensating defects and how they are distributed in a crystal. Clearly, the distribution changes for CaF_2:Yb because the AE is suppressed after X-ray exposure at 200 K plus warming to room temperature, and the AE remains suppressed for at least 8 months. From the calculations, an important issue is the distribution of F_i^- interstitials about the dopant. When the sample is cooled from a high melting temperature, it could lead to a quenched-in distribution that is different from the distribution after X-ray exposure plus warming to room temperature. Even the distribution after a short anneal at 900 K is likely different as the AE has a different shape. Are all of these distributions metastable at 300 K?

These results also raise questions about the many other mixed valence systems with anomalous emission[11] for which charge compensators such as interstitial F^- ions are needed to stabilize the 3+ valence. Are huge, X-ray-induced, valence reductions also found in such systems? In addition, a new challenge arises in finding ways to probe different types of Yb sites (Yb^{2+}, Yb^{3+}_{LC}, Yb^{3+}_{NLC}) and thus better test the interpretations based on the F_i^-/Yb^{3+} and Yb^{2+}/Yb^{3+} charge transfers.

Finally, one important open question remains; if after valence reduction the sample is translated vertically 1 mm, so that the X-ray beam hits a fresh part of the sample, the XANES are the same as a fresh (unreduced) sample, but the AE remains suppressed in the sample entirely. Why is the mechanism for valence reduction so localized, while the anomalous luminescence is quenched in the whole sample?

■ ASSOCIATED CONTENT

Supporting Information

The Supporting Information is available free of charge on the ACS Publications website at DOI: 10.1021/acs.jpcc.7b09161.

Further details about the experiments and the calculations (PDF)

■ AUTHOR INFORMATION

Corresponding Author

*E-mail: bridges@ucsc.edu (F.B.).

ORCID

C. MacKeen: 0000-0003-1167-9728

L. Seijo: 0000-0002-0621-3694

Z. Barandiarán: 0000-0001-7166-6844

M. Kozina: 0000-0002-4747-345X

A. Mehta: 0000-0003-0870-6932

Notes

The authors declare no competing financial interest.

■ ACKNOWLEDGMENTS

The experiments were performed at the Stanford Synchrotron Radiation Lightsource (SSRL), which is supported by the U.S. Department of Energy, Office of Science, Office of Basic Energy Sciences, under Contract DE-AC02-76SF00515. We thank Ryan Davis and Valery Borzenets for help setting up the station for these measurements. L.S. and Z.B. acknowledge Ministerio de Economía y Competitividad, Spain, Dirección General de Investigación y Gestión del Plan Nacional de I+D+i, for Grant MAT2014-54395-P.

■ REFERENCES

(1) McClure, D. S.; Kiss, Z. Survey of the Spectra of the Divalent Rare-earth Ions in Cubic Crystals. *J. Chem. Phys.* **1963**, *39*, 3251−3257.

(2) DeLoach, L. D.; Payne, S. A.; Chase, L. L.; Smith, L. K.; Kway, W. L.; Krupke, W. F. Evaluation of Absorption and Emission Properties of Yb^{3+} Doped Crystals for Laser Applications. *IEEE J. Quantum Electron.* **1993**, *29*, 1179−1191.

(3) Krupke, W. F. Ytterbium Solid-state Lasers. The First Decade. *IEEE J. Sel. Top. Quantum Electron.* **2000**, *6*, 1287−1296.

(4) Lucca, A.; Debourg, G.; Jacquemet, M.; Druon, F.; Balembois, F.; Georges, P.; et al. High-power Diode-pumped Yb^{3+}:CaF_2 Femtosecond Laser. *Opt. Lett.* **2004**, *29*, 2767−2769.

(5) Ashurov, M. K.; Boibobeva, S. T.; Nuritdinov, I.; Garibin, E. A.; Demidenko, A. A.; Kuznetsov, S. V.; Fedorov, P. P. Irradiation Behavior of Ytterbium-Doped Calcium Fluoride Crystals and Ceramics. *Inorg. Mater.* **2016**, *52*, 842−850.

(6) Feofilov, P. P. Pogloshchenie i Lyuminestsentsiya Dvukhvalentnykh Ionov Redkikh Zemel v Kristallakh Iskusstvennogo i Prirodnogo Flyuorita. *Opt. Spektrosk.* **1956**, *1*, 992−999.

(7) Kaplyanskii, A. A.; Feofilov, P. P. The Spectra of Divalent Rare Earth Ions in Crystals of Alkaline Earth Fluorides. II. Europium and Ytterbium. *Opt. Spectrosc.* **1962**, *13*, 129−132.

(8) Hughes-Currie, R. B.; Ivanovskikh, K. V.; Wells, J.-P. R.; Reid, M. F.; Gordon, R. A.; Seijo, L.; Barandiarán, Z. X-ray Excitation Triggers Ytterbium Anomalous Emission in CaF_2:Yb but Not in SrF_2:Yb. *J. Phys. Chem. Lett.* **2017**, *8*, 1175−1178.

(9) McClure, D. S.; Pédrini, C. Excitons Trapped at Impurity Centers in Highly Ionic Crystals. *Phys. Rev. B: Condens. Matter Mater. Phys.* **1985**, *32*, 8465−8468.

(10) Moine, B.; Courtois, B.; Pédrini, C. Luminescence and Photoionization Processes of Yb^{2+} in CaF_2, SrF_2 and BaF_2. *J. Phys. (Paris)* **1989**, *50*, 2105−2119.

(11) Dorenbos, P. Anomalous Luminescence of Eu^{2+} and Yb^{2+} in Inorganic Compounds. *J. Phys.: Condens. Matter* **2003**, *15*, 2645−2665.

(12) Barandiarán, Z.; Seijo, L. Intervalence Charge Transfer Luminescence: Interpaly Between Anomalous and $5d-4f$ Emissions in Yb-Doped Florite-Type Crystals. *J. Chem. Phys.* **2014**, *141*, 234704.

(13) Hughes-Currie, R. B.; Ivanovskikh, K. V.; Wells, J.-P. R.; Reid, M. F.; Gordon, R. A. The Determination of Dopant Ion Valence Distributions in Insulating Crystals Using XANES Measurements. *J. Phys.: Condens. Matter* **2016**, *28*, 135502.

(14) MacKeen, C.; Bridges, F.; Kozina, M.; Mehta, A.; Reid, M. F.; Wells, J.-P. R.; Barandiarán, Z. Evidence That the Anomalous Emission from CaF_2:Yb^{2+} Is Not Described by the Impurity Trapped Exciton Model. *J. Phys. Chem. Lett.* **2017**, *8*, 3313−3316.

(15) Welber, B. Reversible Phototransfer of Electrons between Rare-Earth Ions in CaF_2. *J. Chem. Phys.* **1965**, *42*, 4262−4264.

(16) Kaczmarek, S. M.; Tsuboi, T.; Ito, M.; Boulon, G.; Leniec, G. Optical Study of Yb^{3+}/Yb^{2+} Conversion in CaF_2 Crystals. *J. Phys.: Condens. Matter* **2005**, *17*, 3771−3786.

(17) Petit, V.; Camy, P.; Doualan, J.-L.; Portier, X.; Moncorgé, R. Spectroscopy of Yb^{3+}:CaF_2: From Isolated Centers to Clusters. *Phys. Rev. B: Condens. Matter Mater. Phys.* **2008**, *78*, 085131.

(18) Nicoara, I.; Lighezan, L.; Enculescu, M.; Enculescu, I. Optical Spectroscopy of Yb^{2+} Ions in YbF_3-doped CaF_2 Crystals. *J. Cryst. Growth* **2008**, *310*, 2026−2032.

(19) Merz, J. L.; Pershan, P. S. Charge Conversion of Irradiated Rare-Earth Ions in Calcium Fluoride. I. *Phys. Rev.* **1967**, *162*, 217−235.

(20) Merz, J. L.; Pershan, P. S. Charge Conversion of Irradiated Rare-Earth Ions in Calcium Fluoride. II. Thermoluminescent Spectra. *Phys. Rev.* **1967**, *162*, 235−247.

(21) Booth, C. H. R-Space X-ray Absorption Package. 2010; http://lise.lbl.gov/RSXAP/.

(22) Hughes-Currie, R. B.; Ivanovskikh, K. V.; Wells, J.-P. R.; Reid, M. F.; Gordon, R. A. The Determination of Dopant Ion Valence

DOI: 10.1021/acs.jpcc.7b09161
J. Phys. Chem. C 2017, 121, 28435−28442

Distributions in Insulating Crystals Using XANES Measurements. *J. Phys.: Condens. Matter* **2016**, *28*, 135502.
(23) Douglas, M.; Kroll, N. M. Quantum Electrodynamical Corrections to the Fine Structure of Helium. *Ann. Phys. (Amsterdam, Neth.)* **1974**, *82*, 89−155.
(24) Hess, B. A. Relativistic Electronic-Structure Calculations Employing a Two-Component No-Pair Formalism with External-Field Projection Operators. *Phys. Rev. A: At., Mol., Opt. Phys.* **1986**, *33*, 3742−3748.
(25) Hess, B. A.; Marian, C. M.; Wahlgren, U.; Gropen, O. A Mean-Field Spin-Orbit Method Applicable to Correlated Wavefunctions. *Chem. Phys. Lett.* **1996**, *251*, 365−371.
(26) Barandiarán, Z.; Seijo, L. The Ab Initio Model Potential Representation of the Crystalline Environment. Theoretical Study of the Local Distortion on NaCl:Cu^{+}. *J. Chem. Phys.* **1988**, *89*, 5739−5746.
(27) Seijo, L.; Barandiarán, Z. In *Computational Chemistry: Reviews of Current Trends*; Leszczyński, J., Ed.; World Scientific: Singapore, 1999; Vol. *4*, pp 55−152.
(28) Gellé, A.; Lepetit, M.-B. Fast Calculation of the Electrostatic Potential in Ionic Crystals by Direct Summation Method. *J. Chem. Phys.* **2008**, *128*, 244716.
(29) Roos, B. O.; Lindh, R.; Malmqvist, P. A.; Veryazov, V.; Widmark, P. O.; Borin, A. C. New Relativistic Atomic Natural Orbital Basis Sets for Lanthanide Atoms with Applications to the Ce Diatom and LuF_3. *J. Phys. Chem. A* **2008**, *112*, 11431−11435.
(30) Roos, B. O.; Taylor, P. R.; Siegbahn, P. E. M. A Complete Active Space SCF Method (CASSCF) Using a Density-Matrix Formulated Super-CI Approach. *Chem. Phys.* **1980**, *48*, 157−173.
(31) Siegbahn, P. E. M.; Heiberg, A.; Almlöf, J.; Roos, B. O. The Complete Active Space SCF (CASSCF) Method in a Newton-Raphson Formulation with Application to the HNO Molecule. *J. Chem. Phys.* **1981**, *74*, 2384−2396.
(32) Olsen, P. J.; Roos, B. O.; Jensen, J. A. Determinant Based Configuration-Interaction Algorithms for Complete and Restricted Configuration-Interaction Spaces. *J. Chem. Phys.* **1988**, *89*, 2185.
(33) Malmqvist, P.-A.; Rendell, A.; Roos, B. O. The Restricted Active Space Self-Consistent-Field Method, Implemented with a Split Graph Unitary-Group Approach. *J. Phys. Chem.* **1990**, *94*, 5477−5482.
(34) Malmqvist, P.-Å.; Pierloot, K.; Moughal Shahi, A. R.; Cramer, C. J.; Gagliardi, L. The Restricted Active Space Followed by Second-Order Perturbation Theory Method: Theory and Application to the Study of CuO_2 and Cu_2O_2 Systems. *J. Chem. Phys.* **2008**, *128*, 204109.
(35) Andersson, K.; Malmqvist, P.-A.; Roos, B. O.; Sadlej, A. J.; Wolinski, K. Second-Order Perturbation Theory with a CASSCF Reference Function. *J. Phys. Chem.* **1990**, *94*, 5483−5488.
(36) Andersson, K.; Malmqvist, P.-A.; Roos, B. O. Second-Order Perturbation Theory with a Complete Active Space Self-Consistent Field Reference Function. *J. Chem. Phys.* **1992**, *96*, 1218−1226.
(37) Zaitsevskii, A.; Malrieu, J.-P. Multi-Partitioning Quasidegenerate Perturbation Theory. A New Approach to Multireference Møller-Plesset Perturbation Theory. *Chem. Phys. Lett.* **1995**, *233*, 597−604.
(38) Finley, J.; Malmqvist, P.-A.; Roos, B. O.; Serrano-Andrés, L. The Multi-State CASPT2Method. *Chem. Phys. Lett.* **1998**, *288*, 299−306.
(39) Karlström, G.; Lindh, R.; Malmqvist, P. A.; Roos, B. O.; Ryde, U.; Veryazov, V.; Widmark, P. O.; Cossi, M.; Schimmelpfennig, B.; Neogrady, P.; et al. MOLCAS: a Program Package for Computational Chemistry. *Comput. Mater. Sci.* **2003**, *28*, 222−239.
(40) Chen, H.; He, X.; Sheng, C.; Ma, Y.; Nie, H.; Xia, W.; Ying, W. Interactions Between Synchrotron Radiation X-ray and Biological Tissues - Theoretical and Clinical Significance. *Int. J. Physiol. Pathophysiol. Pharmacol.* **2011**, *3*, 243−248.
(41) Gianoncelli, A.; Vaccari, L.; Kourousias, G.; Cassese, D.; Bedolla, D. E.; Kenig, S.; Storici, P.; Lazzarino, M.; Kiskinova, M. Soft X-Ray Microscopy Radiation Damage On Fixed Cells Investigated With Synchrotron Radiation FTIR Microscopy. *Sci. Rep.* **2015**, *5*, 10250.
(42) Kumar, R. S.; Svane, A.; Vaitheeswaran, G.; Zhang, Y.; Kanchana, V.; Hofmann, M.; Campbell, S. J.; Xiao, Y.; Chow, P.; Chen, C.; et al. Pressure-Induced Valence and Structural Changes in $YbMn_2Ge_2$ - Inelastic X-ray Spectroscopy and Theoretical Investigations. *Inorg. Chem.* **2013**, *52*, 832−839.
(43) Antonio, M. R.; Soderholm, L.; Song, I. Design of Spectroelectrochemical Cell for In Situ X-ray Absorption and Structure Measurements of Bulk Solution Species. *J. Appl. Electrochem.* **1997**, *27*, 784−792.
(44) Ankudinov, A. L.; Rehr, J. J. Relativistic Calculations of Spin-Dependent X-ray-Absorption Spectra. *Phys. Rev. B: Condens. Matter Mater. Phys.* **1997**, *56*, R1712−R1715.
(45) Bridges, F.; Castillo-Torres, J.; Car, B.; Medling, S.; Kozina, M. EXAFS Evidence for a Primary Zn_{Li} Dopant in $LiNbO_3$. *Phys. Rev. B: Condens. Matter Mater. Phys.* **2012**, *85*, 064107.
(46) Görlich, P.; Karras, H.; Symanowski, C.; Ullmann, P. The Colour Centre Absorption of X-ray Coloured Alkaline Earth Fluoride Crystals. *Phys. Status Solidi B* **1968**, *25*, 93−101.
(47) Friedman, E.; Low, W. Effect of Thermal Treatment of Paramagnetic Resonance Spectra of Rare Earth Impurities in Calcium Fluoride. *J. Chem. Phys.* **1960**, *33*, 1275−1276.
(48) Sierro, J. Paramagnetic Resonance of Gd^{3+} in SrF_2 and BaF_2. *Phys. Lett.* **1963**, *4*, 178−180.
(49) Barandiarán, Z.; Meijerink, A.; Seijo, L. Configuration Coordinate Energy Level Diagrams of Intervalence and Metal-to-Metal Charge Transfer States of Dopant Pairs in Solids. *Phys. Chem. Chem. Phys.* **2015**, *17*, 19874−19884.
(50) Barandiarán, Z.; Seijo, L. Metal-to-Metal Charge Transfer Between Dopant and Host Ions: Photoconductivity of Yb-Doped CaF_2 and SrF_2 crystals. *J. Chem. Phys.* **2015**, *143*, 144702.
(51) Sugar, J.; Spector, N. Spectrum and Energy Levels of Doubly Ionized Europium (Eu III). *J. Opt. Soc. Am.* **1974**, *64*, 1484−1497.
(52) Kaufman, V.; Sugar, J. Wavelengths, Classifications, and Ionization Energies in the Isoelectronic Sequences from Yb II and Yb III through Bi XV and Bi XVI. *J. Opt. Soc. Am.* **1976**, *66*, 1019−1025.
(53) Martin, W. C.; Zalubas, R.; Hagan, L. *Atomic Energy Levels - The Rare Earth Elements*; Natl. Stand. Ref. Data Ser., Natl. Bur. Stand. No. 60; U.S. GPO: Washington, DC, 1978.

DOI: 10.1021/acs.jpcc.7b09161
J. Phys. Chem. C 2017, 121, 28435−28442